


## Tuning superconductivity in Ge:Ga using Ga<sup>+</sup> implantation energy

Kasra Sardashti,<sup>1</sup> Tri D. Nguyen,<sup>1,2</sup> Wendy L. Sarney,<sup>3</sup> Asher C. Leff,<sup>3</sup> Mehdi Hatefipour,<sup>1</sup> Matthieu C. Dartiailh,<sup>1</sup> Joseph Yuan,<sup>1</sup> William Mayer,<sup>1</sup> and Javad Shabani<sup>1</sup>

<sup>1</sup>Center for Quantum Phenomena, Department of Physics, New York University, New York 10003, USA

<sup>2</sup>Department of Physics, City College of New York, City University of New York, New York 10031, USA

<sup>3</sup>CCDC U.S. Army Research Laboratory, Adelphi, Maryland 20783, USA

 (Received 12 November 2020; revised 17 March 2021; accepted 25 May 2021; published 22 June 2021)

High-fluence gallium (Ga<sup>+</sup>) implantation at medium energies is proven to be an effective tool in forming superconducting (SC) thin films in germanium (Ge). By changing the post-implantation annealing conditions nanocrystalline to single-crystalline Ge matrices have been produced. Irrespective of crystallinity, such processes have mostly led to supersaturated Ge:Ga films where superconductivity is controlled by the extent of coherent coupling between Ga precipitates. Here we use Ga<sup>+</sup> implantation energy as a means to tailor the spatial distribution and the coupling energy of the Ga precipitates. By systematic structural and magneto-transport studies, we unravel the complex connection between the internal structure of Ge:Ga films and their global SC parameters. At the shallowest implantation depth, we observe the strongest coupling leading to a robust superconductivity that sustains parallel magnetic fields as high as 9.95 T, above the conventional Pauli paramagnetic limit and consistent with a quasi-2D geometry. Further measurements at mK temperatures revealed an anomalous upturn in perpendicular critical field  $B_{\perp}$  vs temperature whose curvature and thus origin may be tuned between weakly coupled SC arrays and vortex glass states with quenched disorder. This warrants future investigations into Ge:Ga films for applications where tunable disorder is favorable, including test-beds for quantum phase transitions and superinductors in quantum circuits.

DOI: [10.1103/PhysRevMaterials.5.064802](https://doi.org/10.1103/PhysRevMaterials.5.064802)

### I. INTRODUCTION

Group IV semiconductors are favored for integration into hybrid semiconductor-superconductor (Sm-S) quantum circuits due to their high purity and compatibility with the highly scalable complementary metal-oxide-semiconductor technologies [1,2]. Germanium (Ge) is particularly compelling for hybrid S-Sm devices because ultraclean materials with high hole mobility can be achieved [3]. Realizing superconductivity in Ge is believed to facilitate its integration into superconducting (SC) circuits. Similar to silicon (Si) [4–6], SC phases of Ge have been demonstrated by incorporating large amounts of gallium (Ga) into its lattice [7,8]. For this purpose, Ge substrates underwent medium-energy (i.e., 100 keV) Ga<sup>+</sup> implantation with fluxes on the order of  $10^{16}$  cm<sup>-2</sup> (~5–8 at.% Ga), followed by annealing at temperatures near the melting point of Ge (~938 °C) [7–10]. Such high concentrations of Ga can dope Ge beyond metal-insulator transition limits, narrow the band gap, and induce superconductivity in hyperdoped crystals [11,12]. But since Ga has low solubility in Ge (maximum of ~1.1% at about 700 °C), its precipitation within the implanted films may be inevitable [13]. Therefore, beside hyperdoping, coherent Josephson coupling between SC Ga precipitates can contribute to the global superconductivity in Ge:Ga films [14,15].

In the quest to isolate the effect of hyperdoping on Ge:Ga superconductivity, the near entirety of the efforts so far have focused on controlling the Ga precipitation at a fixed im-

plantation energy ( $E_{\text{IMP}}$ ) of 100 keV by using the activation annealing conditions (e.g., temperature, time, and heating technique) as the primary tuning parameters [7–10,16,17]. Those studies have successfully produced SC Ge:Ga films with nano-, poly-, and single-crystalline Ge matrices. In the single-crystalline phase, one expects Ga hyperdoping to be the predominant superconductivity mechanism since minimal microscopic precipitates were observed. However, even at this limit the dopant activation efficiency of only 31.5% was reported for Ga bearing the question as for the contribution of the remaining 68.5% Ga to the superconductivity [10]. Although many efforts have been focused on nullifying the effect of Ga precipitation in Ge, the distributed nature of its superconductivity controlled by the extent of coherent coupling within and in between Ga clusters provides an interesting platform to tune the superconductivity, particularly for applications where high disorder in a short-length scale is favorable [14,15,18].

In this work, we use Ga<sup>+</sup> implantation energy  $E_{\text{IMP}}$  as a parameter to tune the Ga distribution within Ge:Ga thin films. By varying activation annealing temperatures ( $T_{\text{DA}}$ ) at each energy, we show a wide  $E_{\text{IMP}}-T_{\text{DA}}$  processing phase space over which global superconductivity in Ge:Ga can be tuned. Through systematic structural and magneto-transport characterization of our Ge:Ga samples, we demonstrate how the distribution as well as the intercluster coupling of Ga precipitates determine the eventual SC properties of the films. At the shallowest implantation depth, we observe

the strongest coupling leading to a robust superconductivity that sustains parallel magnetic fields above the conventional Pauli paramagnetic limit, consistent with a quasi-2D geometry. Furthermore, pronounced crossing zones in the magnetoresistance curves of the films with low  $E_{\text{IMP}}$  points to disordered systems that potentially host quantum phase transitions (QPTs) [19,20]. Measurements at mK temperatures showed anomalous upturn in perpendicular critical field ( $B_c$ ) vs temperature, pointing to the presence of quenched disorder and vortex glass states. These signatures warrant future investigations into Ge:Ga films for a rather unconventional range of applications such as superinductors [21], magnetic-field-resistant SC resonators [22,23], and phase-slip qubits [24,25].

## II. EXPERIMENTAL DETAILS

### A. Materials Synthesis

Undoped Ge(100) wafers grown by the floating zone method with room-temperature resistivity of  $40 \Omega \cdot \text{cm}$  were used. Prior to implantation, Ge native oxide was etched using cyclic immersion in 10% HF solution and DI- $\text{H}_2\text{O}$ . This was followed by the deposition of 30-nm thick  $\text{SiO}_2$  top barriers via plasma-enhanced chemical vapor deposition. The oxide barrier helps minimize direct damage to the Ge substrates during the ion implantation process.  $\text{Ga}^+$  ion implantation processes (by Kroko Inc.) were carried out at 25, 35, 45, and 80 keV with a fixed ion fluence of  $4 \times 10^{16} \text{ cm}^{-2}$ . Throughout implantation substrates were held at room temperature. After implantation dopants were activated using rapid thermal annealing under 5 standard liter per minute of  $\text{N}_2$  flow and at 300 to 800 °C for 1 min.

### B. Transport Measurements

Electrical properties of the samples were evaluated by measuring the differential resistance (i.e.,  $dV/dI$ ), using lock-in amplifiers, for  $5 \text{ mm} \times 5 \text{ mm}$  samples in Van der Pauw geometry. The AC excitation current for the measurements varied between 1 and  $20 \mu\text{A}$ . Measurements from room temperature ( $\sim 300 \text{ K}$ ) down to 1.5 K were performed in a Teslatron PT (Oxford Instruments) cryogen-free refrigerator with maximum magnetic field of 12 T (along the  $z$  axis). Measurements below 1.2 K were carried out in a Triton dilution refrigerator (Oxford Instruments) with a 3-axis vector magnet and maximum  $z$  field of 6T. Hall measurements were performed on L-shaped bars. Hall bars were fabricated by UV photolithography followed by reactive ion etching of the mesa using  $\text{CF}_4/\text{O}_2$  gas mixtures for 2–5 min. The resulting mesa heights varied between 500 and  $1.2 \mu\text{m}$  (further details are in the Supplemental Material).

### C. Structural and Chemical Characterization

Micro-Raman spectroscopy was performed using a Horiba Xplora  $\mu$ -Raman system with a 532-nm excitation laser and an objective lens of  $1000\times$  magnification. Atomic force microscopy (AFM) was performed in order to determine the surface morphology of the SC films in details. A Bruker Dimension Fastscan scanning probe microscopy system was used in tapping mode (ScanAsyst mode). The AFM probes

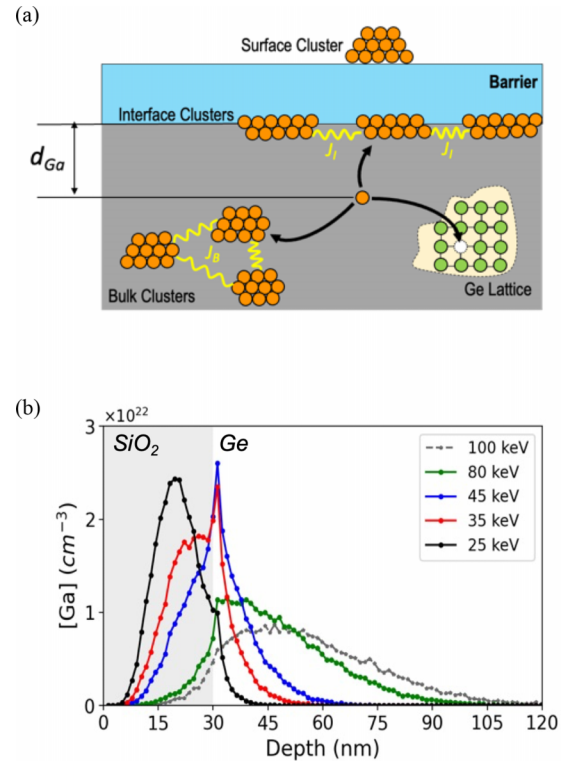


FIG. 1. (a) A schematic detailing the various pathways implanted Ga atoms can take within the Ge matrix, including substituting Ge as a dopant, precipitation within the implanted region, precipitation at the  $\text{SiO}_2/\text{Ge}$  interface, and finally diffusion through the  $\text{SiO}_2$  to form Ga surface clusters. The yellow squiggly lines represent the nearest-neighbor coupling between the Ga clusters within the bulk ( $J_B$ ) or at the interface ( $J_I$ ). (b) One-dimensional simulation of Ga concentration vs depth for various implantation energies from 25 to 100 keV, calculated by TRIM for  $\text{Ga}^+$  fluence of  $4 \times 10^{16} \text{ cm}^{-2}$ .

used for the measurements were Bruker FASTSCAN-B, made of Si nitride with triangular tips of 5–12 nm radius.

### D. Electron Microscopy

The crystal morphology of the structures was examined with transmission electron microscopy (TEM) in a JEOL ARM200F, equipped with a spherical aberration corrector for probe mode, and operated at 200 keV. The composition of each films was studied with energy-dispersive x-ray spectroscopy (EDS). The samples were prepared with cross-sectional tripod polishing to  $20 \mu\text{m}$  thickness, followed by shallow angle  $\text{Ar}^+$  ion milling with low beam energies ( $\leq 3 \text{ keV}$ ), and  $\text{LN}_2$  stage cooling in a PIPS II ion mill.

## III. RESULTS AND DISCUSSION

### A. Transport properties vs processing conditions

Figure 1(a) displays the pathways Ga ions may take within a Ge substrate during the activation annealing. The  $\text{SiO}_2$  barrier depicted on top of the Ge substrate is commonly used to prevent surface damage during ion implantation. Due to low solubility, beside occupying Ge sites as a p-type dopant,

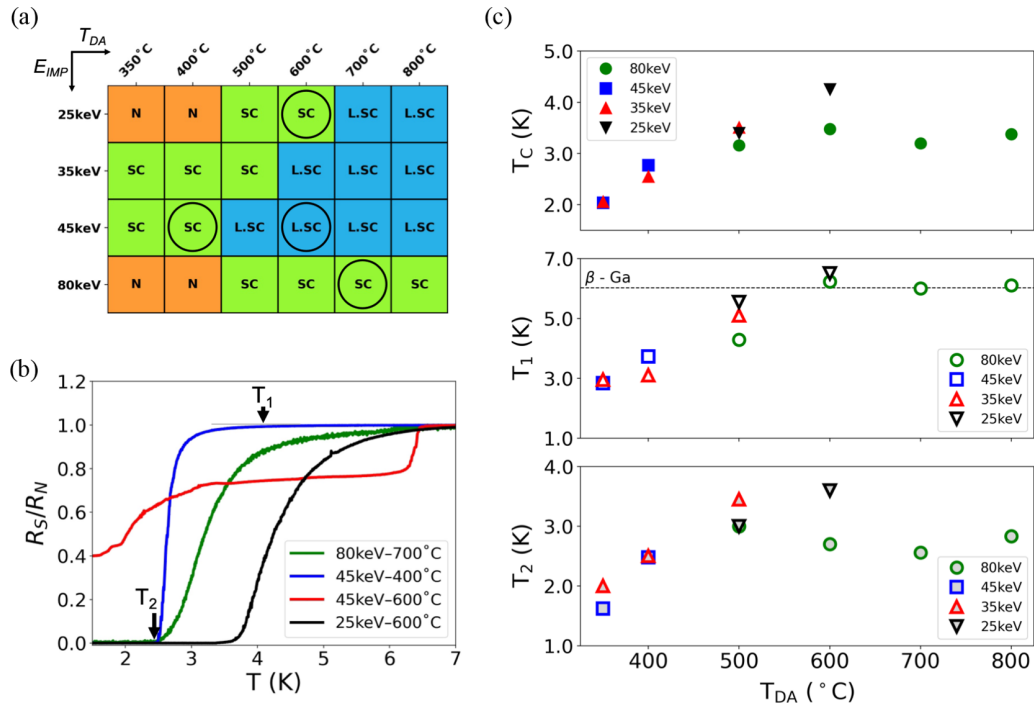


FIG. 2. (a) An overview of transport properties, marked by “N,” normal; “SC,” superconducting; and “L.SC,” locally superconducting vs processing conditions used in this study, i.e., implantation energy  $E_{IMP}$  and annealing temperature  $T_{DA}$ . (b) Sheet resistance  $R_S$  (normalized to sheet resistance at 9K,  $R_N$ ) vs temperature showing SC transitions for four representative processing conditions circled in (a). Transition onset and completion temperatures for the blue curve are marked as  $T_1$  and completion  $T_2$ , respectively. (c) Superconducting transition midpoint  $T_c$  (at  $R_S = 0.5 R_N$ ), onset  $T_1$ , and completion  $T_2$  vs anneal temperature  $T_{DA}$  for samples with complete zero-resistance transitions. The  $T_c$  value for  $\beta$ -Ga is adapted from Ref. [26].

Ga could precipitate within the implanted region (into bulk clusters) or at the Ge/SiO<sub>2</sub> interface (into interface clusters). At high enough temperatures Ga may even diffuse through the SiO<sub>2</sub> barrier to form surface clusters. The percentage of implanted Ga atoms participating in each process is expected to depend on their depth distribution within the Ge matrix, which in turn is a function of  $E_{IMP}$ . Using the Transport of Ions In Matter (TRIM) Monte Carlo software [27], we simulated the Ga depth distribution for  $E_{IMP} = 25$  to 100 keV [Fig. 1(b)]. The simulation results show that reducing  $E_{IMP}$  shifts the Ga distribution peak closer to the top surface enabling stronger Ga confinement near the Ge/SiO<sub>2</sub> interface. This should enable formation of constricted arrays of coupled interface Ga clusters with critical SC parameters well beyond those reported for Ge:Ga so far. It should be noted that  $E_{IMP} = 100$  keV is the only value used in previous reports of Ge:Ga superconductivity [8,10,17,28].

Our Ge:Ga films were prepared at  $E_{IMP} = 25$ –80 keV and underwent annealing in a wide temperature range from 300 to 800°C. Figure 2(a) shows the  $E_{IMP}$ – $T_{DA}$  processing phase space for the Ge:Ga samples prepared in this study. Three groups of samples were identified based on the temperature-dependence of their resistance including: (i) Superconducting (SC) with transitions to a zero-resistance state; (ii) normal (N) with finite resistance and no clear transition down to 1.5 K; (iii) samples with localized superconductivity (L.SC) as evidenced by a clear drop in resistance at 6–7 K, yet finite resistance at 1.5 K. The difference between the complete and localized superconductivity is highlighted by resistance mea-

surements shown in Fig. 2(b). Here, four samples are shown that are representative of superconductivity with different Ga depth distributions (see Supplemental Fig. S1 for complete resistance measurement data for all processing conditions [29]). The red curve represents a sample with a partial SC transition at 6.5 K, close to the  $T_c$  observed for confined Ga layers in Si [4,6]. This behavior may be ascribed to SC Ga clusters that are spaced beyond the length scale necessary for their coherent coupling [15,30]. On the other hand, for samples with complete SC transitions,  $T_c$  in Ge:Ga does not reach the values for Si:Ga (6–7.5 K), consistent with the presence of proximitized regions with  $T_c \approx \Delta \exp[-d/\xi_N(T_c)]$  following the Lobb, Abraham, and Thinkham model [31], where  $\Delta$  is the Ga SC gap and  $\xi_N$  is the normal coherence length in Ge.

As shown in Fig. 2(b), for SC Ge:Ga films, in addition to the conventional critical temperature  $T_c$  (at  $R_S/R_N = 0.5$ ), we follow the temperatures for the onset ( $T_1$ ) and the completion ( $T_2$ ) of the transitions.  $T_1$  and  $T_2$  are defined in analogy to the mesoscopic superconductor-metal array model, assuming that Ga clusters separated by heavily doped p-Ge are the main contributors to the superconductivity [18,32]. According to this model,  $T_1$  represents the phase coherence within the clusters, which depends on their structural state.  $T_2$  shows the extent of intercluster coupling (i.e.,  $J_B, J_I$ ) that is depends on the distance between the clusters and the normal coherence length ( $\xi_N$ ) of the p-Ge channels. Figure 2(c) displays plots of  $T_c$ ,  $T_1$ , and  $T_2$  vs  $T_{DA}$  at four different implantation energies. When  $T_{DA} \geq 600$  °C,  $T_1$  appears to reach an upper limit near the SC transition temperature for  $\beta$ -Ga, consistent



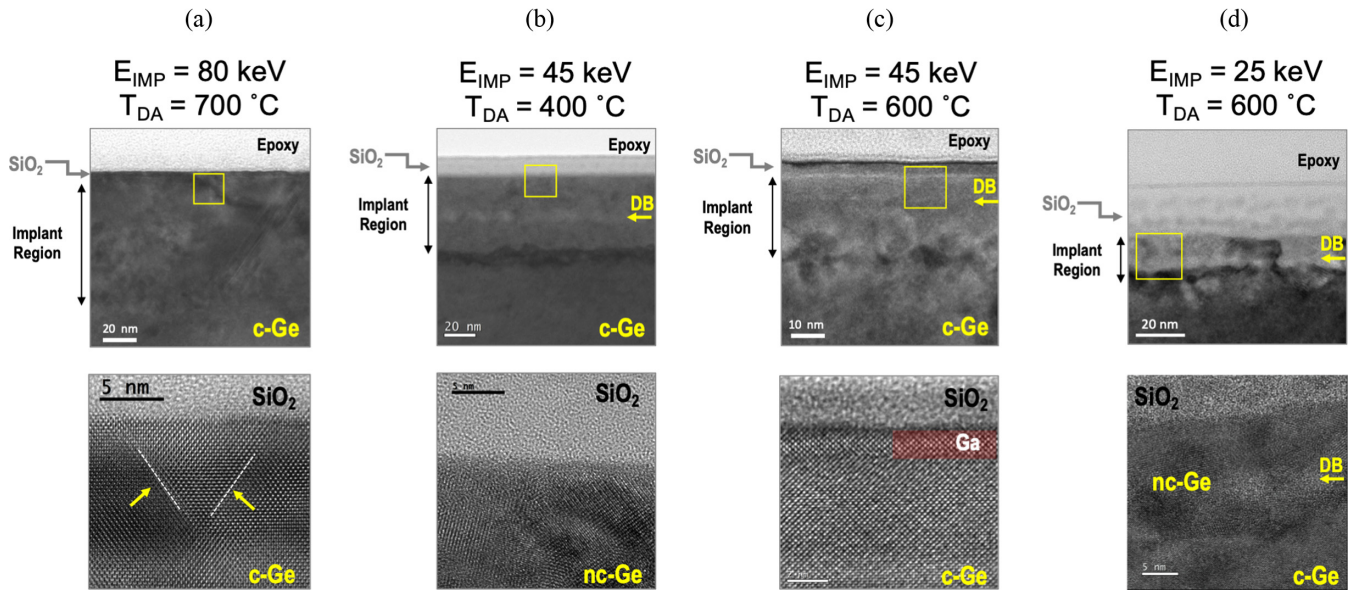


FIG. 3. TEM images of cross-sections prepared on Ge:Ga samples with (a)  $E_{\text{IMP}} = 80$  keV and  $T_{\text{DA}} = 700$  °C; (b)  $E_{\text{IMP}} = 45$  keV and  $T_{\text{DA}} = 400$  °C; (c)  $E_{\text{IMP}} = 45$  keV and  $T_{\text{DA}} = 600$  °C; (d)  $E_{\text{IMP}} = 25$  keV and  $T_{\text{DA}} = 600$  °C. The yellow boxes shown in lower magnification images (top row) are visual guides to outline the approximate areas from which the higher magnification images (bottom row) were taken. In (a), the dotted lines denote stacking faults within the Ge after dopant activation annealing. In (b)–(d), “DB” are seen as a result of  $\text{SiO}_2$  recoil during the implantation process.

with the precipitation of phase-coherent  $\beta$ -Ga clusters. At  $T_{\text{DA}} = 600$  °C, we see superconductivity at both  $E_{\text{IMP}} = 25$  and  $80$  keV. Nevertheless, the former  $E_{\text{IMP}}$ , which results in the shallowest Ga depth profile with Ga clusters in close proximity, has the highest  $T_2$  of  $3.6$  K; thus, a more robust SC state is expected at  $E_{\text{IMP}} = 25$  keV and  $T_{\text{DA}} = 600$  °C. This phase also has a  $T_c$  of  $4.25$  K, which is more than  $1$  K above the record value reported for Ge:Ga [7]. Finally, we note for other energies, including  $E_{\text{IMP}} = 35$  and  $45$  keV, the annealing window for superconductivity falls below  $600$  °C. In this regime, wider tunability ranges for  $T_1$  and  $T_2$  are observed as both the crystallinity and the spatial distribution of Ga clusters are sensitive to  $T_{\text{DA}}$ .

To elucidate the role Ga-doping plays in the global superconductivity of the Ge:Ga films, we measured the density of holes ( $n_h$ ) for a pair of samples at each energy  $E_{\text{IMP}}$  with two different annealing temperatures  $T_{\text{DA}}$ , one with complete SC transition and the other with local or no superconductivity. Details of the Hall measurements are provided in the Supplemental Material (Supplemental Fig. S2; Supplemental Table S1 [29]). Overall, superconductivity appears over a wide range of hole densities from  $3.41 \times 10^{15}$  to  $1.07 \times 10^{16}$   $\text{cm}^{-2}$ . However, higher  $n_h$  does not translate to superconductivity as seen in the pairs of samples with  $E_{\text{IMP}} = 35$  and  $45$  keV. In the former, an increase in  $T_{\text{DA}}$  raised  $n_h$  from  $5.70 \times 10^{15}$   $\text{cm}^{-2}$  to  $1.42 \times 10^{16}$   $\text{cm}^{-2}$ , but resulted in loss of the superconductivity. In the latter, annealing at higher  $T_{\text{DA}}$  raised  $n_h$  from  $5.77 \times 10^{15}$   $\text{cm}^{-2}$  to  $1.66 \times 10^{16}$   $\text{cm}^{-2}$ , identically destroying the zero-resistance state above  $1.5$  K. Therefore, in our processing phase space, we infer superconductivity not to stem from hyperdoping of Ge:Ga effects. Instead, Ga doping affects the intercluster coupling  $J$  by changing the conductivity of the Ge matrix surrounding the Ga precipitates. Ga doping of Ge influences hole mobility ( $\mu_h$ ), hole diffusion constant ( $D$ ),

and consequently  $\xi_N(T) = \sqrt{\hbar D/k_B T}$ . This in turn controls the intercluster coupling, which has the standard proximity form of  $J_0 \exp[-d/\xi_N(T)]$  with  $d$  being the average intercluster spacing [31,33].

## B. Structural and compositional characterization

To study the influence of  $E_{\text{IMP}}$  and  $T_{\text{DA}}$  on Ge:Ga film structures, Transmission Electron Microscopy (TEM) was performed on the four representative samples already identified in Fig. 2. The high-resolution TEM images for the samples at low and high magnifications are shown in Fig. 3. For the film prepared at  $E_{\text{IMP}} = 80$  keV and  $T_{\text{DA}} = 700$  °C, the implanted region consists of highly crystalline Ge, although with imperfections such as stacking faults [see Fig. 3(a)]. Additionally, at certain locations along the  $\text{SiO}_2/\text{Ge}$  interface large crystalline Ga puddles ( $\geq 25$  nm wide) were found (not shown here). Dark-field optical microscopy images combined with Raman spectroscopy on identical Ge:Ga films confirmed the formation of a polycrystalline structure with several  $\mu\text{m}$ -wide grains (see Supplemental Figs. S3– S5 [29]).

For Ge:Ga samples with  $E_{\text{IMP}} = 45$  keV, shown in Figs. 3(b) and 3(c), the depths of the regions disturbed by the implanting ions appear to be more than  $2\times$  smaller. In addition, disturbed bands (DB)  $\sim 25$  nm below the  $\text{SiO}_2$  caps are present in both samples as a result of Si and O recoil during the implantation. Focusing on the Ge surrounding the DB, annealing at  $400$  °C forms a nanocrystalline film with few-nm-wide grains. In contrast, annealing at  $600$  °C helped recover the crystallinity to a significant level and allowed for the formation of a few monolayers of crystalline Ga at the  $\text{SiO}_2/\text{Ge}$  interface [highlighted in red in Fig. 3(c)]. Such a crystalline Ga layer appears to be discontinuous as evidenced by its absence in other  $\text{SiO}_2/\text{Ge}$  interface regions.

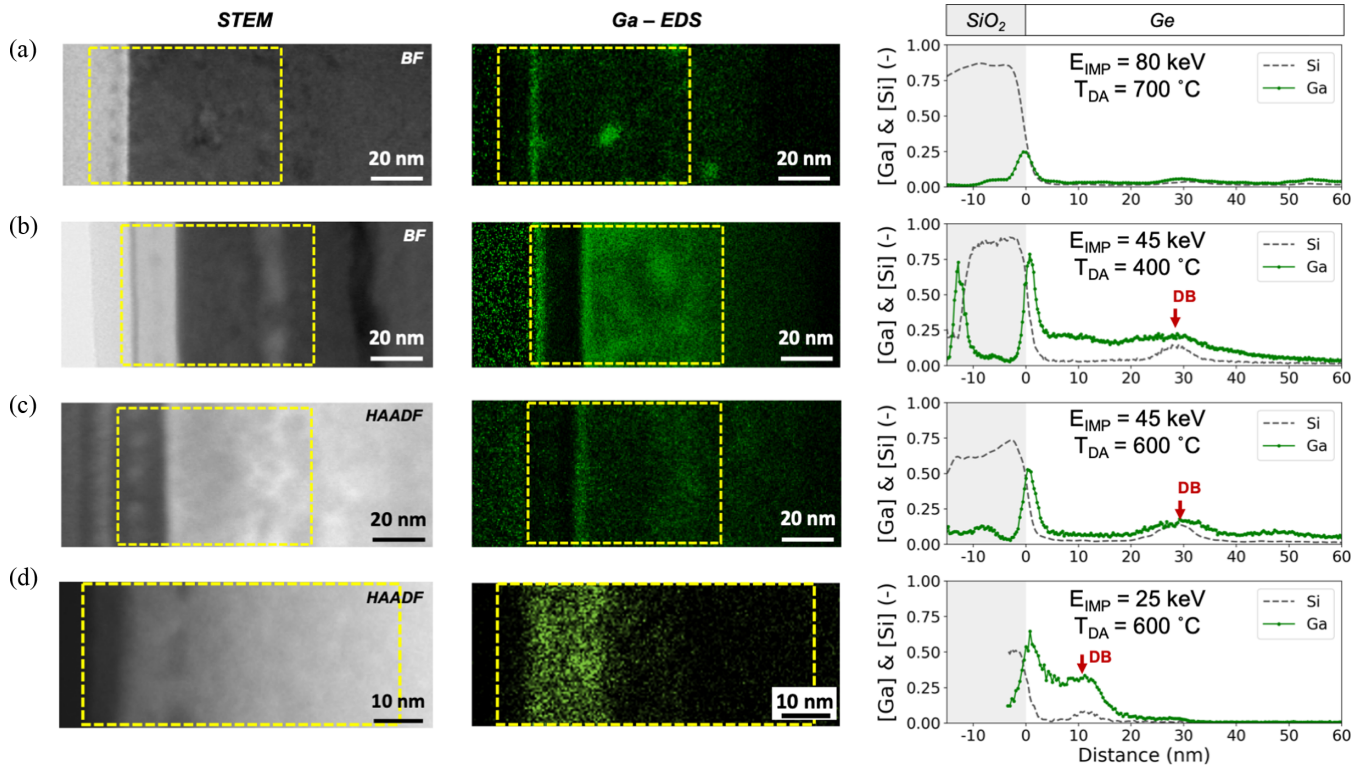


FIG. 4. STEM images and EDS elemental Ga maps for cross-sections of Ga-implanted samples with: (a)  $E_{\text{IMP}} = 80$  keV and  $T_{\text{DA}} = 700$  °C; (b)  $E_{\text{IMP}} = 45$  keV and  $T_{\text{DA}} = 400$  °C; (c)  $E_{\text{IMP}} = 45$  keV and  $T_{\text{DA}} = 600$  °C; (d)  $E_{\text{IMP}} = 25$  keV and  $T_{\text{DA}} = 600$  °C. The line traces for [Ga] (solid green lines) and [Si] (dotted gray lines), normalized to [Si] + [Ge], are shown on the right. The traces are averaged over the width of the areas outlined by the dotted rectangles in the STEM images and maps. The line traces are aligned by setting the  $\text{SiO}_2/\text{Ge}$  interface to zero distance. Disturbed bands are marked by red arrows and “DB.”

This is consistent with the observation of a transition near 6 K ( $\beta$ -Ga transition [26]) to a nonzero resistance state. The difference in the crystallinity of these two systems was confirmed by electron diffraction measurements (see Supplemental Fig. S6 [29]). When  $E_{\text{IMP}}$  is reduced to 25 keV [see Fig. 3(d)], even after annealing at 600 °C, the Ge:Ga films remain nanocrystalline. And while the depth of the implantation region is reduced to only about 20 nm, a DB is present at approximately 12 nm below the  $\text{SiO}_2/\text{Ge}$  interface. This general trend in the crystallinity of the Ge:Ga films was independently confirmed through via dark-field optical microscopy and micro-Raman spectroscopy of all the Ge:Ga samples prepared at various  $E_{\text{IMP}}$  and  $T_{\text{DA}}$  (see Supplemental Figs. S3–S5 [29]).

To better determine the Ga distribution in the samples, the TEM data were complemented by Scanning Transmission Electron Microscopy (STEM) and EDS compositional mapping. Figure 4 shows the STEM images, Ga elemental maps, and line traces for normalized Si and Ga concentrations {i.e.,  $[\text{Ga}] = \text{Ga}\% / (\text{Si}\% + \text{Ge}\%)$ } in the four samples discussed above. For the sample with  $E_{\text{IMP}} = 80$  keV [Fig. 4(a)], the bulk of the implanted region shows [Ga] below 5%, but Ga precipitation is apparent as bulk nanoclusters (diameter  $\sim 5$  nm) and interface clusters near  $\text{SiO}_2/\text{Ge}$ . At  $E_{\text{IMP}} = 45$  keV and  $T_{\text{DA}} = 400$  °C [Fig. 4(b)], in addition to a higher interfacial Ga cluster density, much larger concentrations of Ga ( $\geq 0.2$ ) are evenly distributed within the implanted region. When annealed at 600 °C [Fig. 4(c)], Ga atoms diffuse through the structure both toward the Ge substrate and the

top barrier as evidenced by reduced [Ga] within the implanted region and enhanced [Ga] below the DB. For the sample with  $E_{\text{IMP}} = 25$  keV, where implantation has the shallowest depth [Fig. 4(d)], large amounts of Ga ( $[\text{Ga}] \geq 0.35$ ) are distributed over only a 20 nm-wide region, yet with a significant accumulation the  $\text{SiO}_2/\text{Ge}$  interface. In this case, the distribution region is too thin for the STEM to resolve individual Ga clusters. Moreover, in elemental maps from all samples with  $E_{\text{IMP}} \leq 45$  keV, the presence of the DB is confirmed by the peaks in Si, Ga, and O concentration profiles, consistent with the occurrence of  $\text{SiO}_x$  recoil events for lower  $\text{Ga}^+$  implantation energies (for complete sets of elemental profiles, see Supplemental Fig. S7 [29]). These results confirm that  $E_{\text{IMP}}$  not only changes the Ga depth distribution but also determines its precipitation dynamics at various annealing temperatures. It should also be noted that only small concentrations of Ga ( $[\text{Ga}] \leq 0.15$ ) may be trapped within the bulk of  $\text{SiO}_2$  capping layers. Trapped [Ga] is slightly higher when  $T_{\text{DA}} = 400$  °C due to insufficient thermal energy available for Ga diffusion through amorphous  $\text{SiO}_2$ . Nonetheless, for all annealing temperatures, broad Ga peaks are present at  $\text{SiO}_2/\text{Ge}$  interfaces. Therefore, the Ga interface clusters may be distributed between the Ge substrate and the near-interface region inside the  $\text{SiO}_2$  cap. Distribution of Ga clusters in this manner should contribute to the disorder signatures observed in the global superconductivity of the Ge:Ga films.

The locations of the SC regions in Ge:Ga films are further revealed by etching the  $\text{SiO}_2$  barriers after annealing using

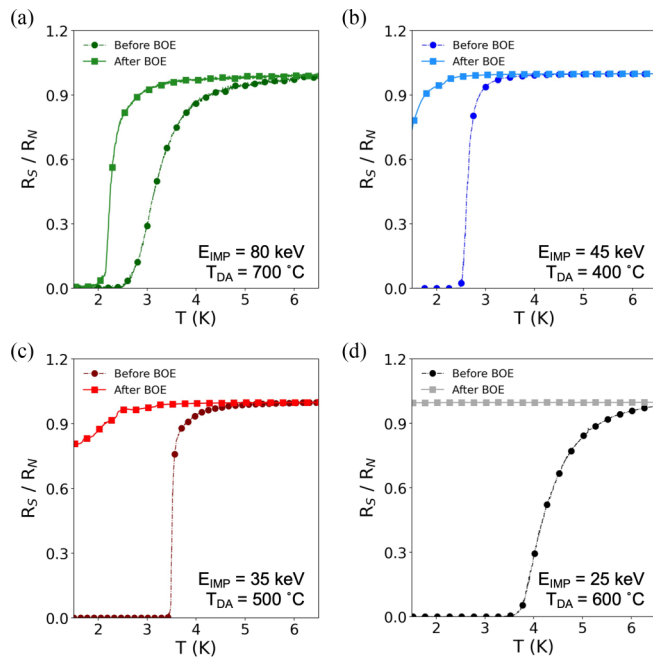


FIG. 5. Normalized resistance vs temperature for four samples before (dash-dotted line) and after etching the  $\text{SiO}_2$  cap (solid line) including: (a)  $E_{\text{IMP}} = 80$  keV and  $T_{\text{DA}} = 700$  °C; (b)  $E_{\text{IMP}} = 45$  keV and  $T_{\text{DA}} = 400$  °C; (c)  $E_{\text{IMP}} = 35$  keV and  $T_{\text{DA}} = 500$  °C; (d)  $E_{\text{IMP}} = 25$  keV and  $T_{\text{DA}} = 600$  °C. For the oxide etch, 15 s dip in 6:1 BOE was followed by 30 s of DI- $\text{H}_2\text{O}$  rinse.

6:1 buffer oxide etchant (BOE). Despite no effect on the microstructure and minimal reactivity with Ga, the etchant is expected to remove Ga through the removal of its host matrix (Ge and  $\text{SiO}_2$ ) [34]. Resistance measurements for four SC samples before and after the BOE etch are shown in Fig. 5. Only the Ge:Ga sample with  $E_{\text{IMP}} = 80$  keV retains its superconductivity after the BOE etch, although with lower  $T_c$  and  $B_c$  (see Supplemental Figs. S8 and S9 for further details [29]). This is consistent with a portion of the superconductivity it from coherent Josephson coupling between the bulk Ga nanoclusters dispersed deeper within the 80–100 nm-deep implanted region [30]. In contrast, for samples with  $E_{\text{IMP}} \leq 45$  keV, the zero-resistance state is destroyed by the BOE. At  $E_{\text{IMP}} = 35$  and 45 keV, some fractions of coupled Ga clusters may still be present deeper in the film as evidenced by the partial resistance dips after the etch. For the sample with  $E_{\text{IMP}} = 25$  keV, however, a fully metallic behavior is observed after the etch, consistent with the picture of complete localization of its superconductive phase near the  $\text{SiO}_2/\text{Ge}$  interface.

### C. Temperature dependence of Resistive Critical Fields

Next, we study the temperature dependence of sheet resistance  $R_S$  in perpendicular ( $B_{\perp}$ ) and parallel ( $B_{\parallel}$ ) magnetic fields as high as 12 T. Figure 6 displays  $R_S$  maps vs temperature and magnetic field for the three representative Ge:Ga films shown in Fig. 2(b) that exhibit complete SC transitions. The resistive critical field ( $B_c$ ) at each temperature is defined as the field at which  $R_S = 0.5 R_n$ . The overlay plots in Fig. 6 indicate temperature dependence of  $B_c$ , which is often known as the boundary for the SC-normal phase transition [14,35]. A

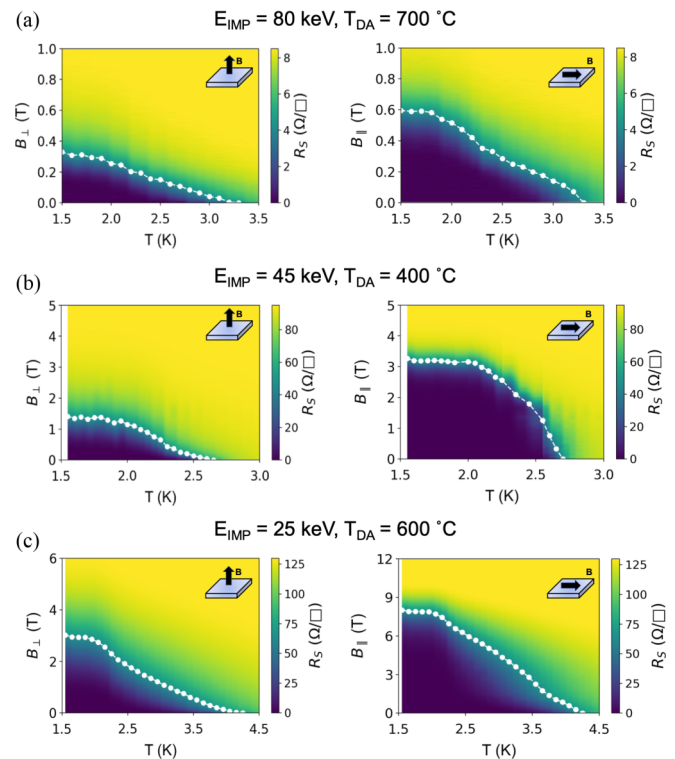


FIG. 6. Sheet resistance maps vs temperature  $T$  and magnetic field applied perpendicular ( $B_{\perp}$ ) and parallel ( $B_{\parallel}$ ) to the surface of the samples prepared at: (a)  $E_{\text{IMP}} = 80$  keV and  $T_{\text{DA}} = 700$  °C; (b)  $E_{\text{IMP}} = 45$  keV and  $T_{\text{DA}} = 400$  °C; (c)  $E_{\text{IMP}} = 25$  keV and  $T_{\text{DA}} = 600$  °C. The white overlay plot on each map outlines the normal-superconductor transition boundary, taken at points where  $R_S = 0.5 R_n$ .

comprehensive version of  $B_c(T)$  phase boundaries for all superconductive Ge:Ga samples is provided in the Supplemental Material (Fig. S10 [29]).

Table I summarizes the key SC parameters extracted from the magneto-transport measurements shown in Figs. 5(a)–5(c). The  $B_c(T)$  phase boundaries outlined in Fig. 5 show significant deviations from the Bardeen-Cooper-Schrieffer and Werthamer-Helfand-Hohenberg models. Therefore, instead of reporting zero-temperature critical magnetic fields ( $B_0$ ), we limit our discussion to  $B_{\perp}$  and  $B_{\parallel}$  at 1.55 K, near the base temperature of our cryostat. Those values are compared to the Pauli paramagnetic limit for the upper critical field, estimated for disordered type-II superconductors as  $B_c$

TABLE I. Summary of SC characteristics for three of the Ge:Ga samples prepared in this study.  $B_{\perp}$  and  $B_{\parallel}$  values are measured at 1.55 K. Coherence length at zero temperature,  $\xi(0)$  is estimated from the linear Ginzburg-Landau relation near  $T_c$ .

$E_{\text{IMP}}$ (keV)	$T_{\text{DA}}$ (°C)	$T_c$ (K)	$B_{\perp}$ (T)	$B_{\parallel}$ (T)	$\xi(0)$ (nm)	$l$ (nm)	$\xi_N(T_2)$ (nm)
80 keV	700	3.3	0.32	0.59	19.7	17	126
45 keV	400	2.65	1.39	3.22	7.0	2.3	47
25 keV	600	4.25	2.97	7.95	6.1	3.3	46



= 1.8  $T_c$  [36,37]. The Ge:Ga film prepared at  $E_{IMP} = 80$  keV has parallel and perpendicular  $B_c$  values well below the Pauli limit of 5.94 T. When  $E_{IMP}$  is lowered to 45 keV we see significant increases in both the perpendicular and the parallel  $B_c$  as they near their Pauli limit of 4.77 T. Finally, when  $E_{IMP} = 25$  keV,  $B_{||}$  surpasses the CC limit of 7.65 T by 0.3 T. Similar behavior has been reported for thin lead films, where the large  $B_c$  is attributed to strong spin-orbit coupling in the 2D metal [38]. This situation may similarly apply to Ge:Ga films with pseudo-2D superconductivity where ultrathin Ga clusters are coupled by heavily doped Ge weak links.

To further evaluate the quality of our Ge:Ga films as a function of  $E_{IMP}$ , we estimated the zero-temperature coherence length,  $\xi(0)$ . In the vicinity of  $T_c$  we observe linear  $B_{\perp}(T)$  behavior for the three samples at  $R(B) = 0.9 R_N$ . We fit the resulting curves to the linear Ginzburg–Landau relationship  $B_{\perp} = \phi_0/[2\pi\xi(0)^2](1 - T/T_c)$ , where  $\phi_0$  is the flux quantum at zero temperature [39]. Using normal sheet resistance  $R_N$  measured at 10 K and carrier concentrations we estimate the mean free path for holes ( $l$ ). All three samples can be identified as “dirty” superconductors since  $\xi(0) > l$ , although reducing  $E_{IMP}$  makes for a dirtier system [ $\xi(0) > 1.5l$ ] as the nanocrystalline Ge matrix becomes the predominant phase after activation annealing. Additionally, by approximating the total thickness of the electrically active region, we determine the bulk hole concentration  $n$ . From  $n$  we obtain the Fermi velocity  $v_F = \hbar/m_h(3\pi^2n)^{1/3}$  and thus the diffusion constant  $D = \frac{1}{3}v_F l$  in the Ge matrix. This leads us to the normal coherence length  $\xi_N(T_2) = \sqrt{\hbar D/k_B T_2}$  as presented in Table I. The larger  $\xi_N(T_2)$  of 126 nm at  $E_{IMP} = 80$  keV shows that coupling could occur between Ga clusters at larger distances; this is consistent with the subsurface superconductive layer observed in this sample. Based on the average Ga cluster distance that could be resolved by electron microscopy ( $\leq 20$  nm), it is rather certain that intercluster spacing  $d$  is much smaller than  $\xi_N(T_2)$  for all samples. This implies the presence of a minimum intercluster coupling  $J \sim J_0 \exp(-d/\xi_N)$  that has to be overcome prior to observing coherent superconductivity across the samples, which may persist even at  $T = 0$  [18]. The higher  $T_c$  and  $T_2$  values for the sample with  $E_{IMP} = 25$  keV confirm that the average  $d$  is much smaller  $\xi_N$ .

Relatively large critical fields with complex temperature dependence are not the only signatures of disordered superconductivity in the Ge:Ga films with shallow Ga profiles. Figures 7(a) and 7(b) display the  $R_s(B)$  isotherms, measured between 1.55 and 3.85 K, for two samples with  $E_{IMP} = 80$  keV and  $T_{DA} = 700$  °C (a), and  $E_{IMP} = 45$  keV and  $T_{DA} = 400$  °C (b). In each sample the crossing points in  $R_s(B)$  were seen at 1.9 and 4 T, respectively. This crossing may be evidence of QPT in quasi-2D disordered superconductors [19,40,41].  $R_s(T)$  behavior vs magnetic field (Supplemental Fig. S11 [29]) indicated a more obvious superconductor-metal transition (SMT) from  $dR/dT < 0$  to  $dR/dT > 0$  for the sample with  $E_{IMP} = 45$  keV. Because of clear SMT along with better-resolved  $R_s(B)$  crossings, we conducted scaling analysis on this sample for the possibility of observing Griffiths singularity with a divergent product of correlation length exponent ( $\nu$ ) and dynamical critical exponent ( $z$ ) [42,43]. Details of scaling analysis are provided in the Supplemental Material (see Supplemental Fig. S12 [29]). For the sample with  $E_{IMP}$

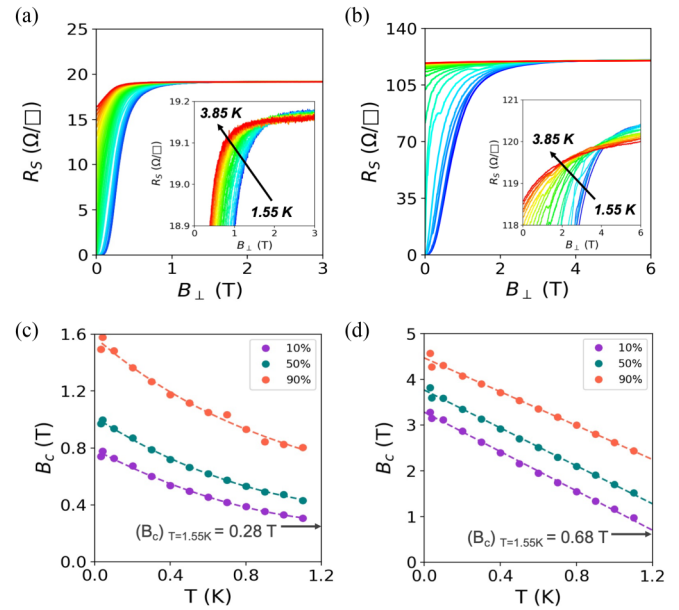


FIG. 7. Magnetoresistance and critical field measurements.  $R_s$  as a function of magnetic field for SC Ge samples with (a)  $E_{IMP} = 80$  keV and  $T_{DA} = 700$  °C and (b)  $E_{IMP} = 45$  keV and  $T_{DA} = 400$  °C at 1.55–3.85 K.  $B_c$  vs temperature extracted from  $R_s(B)$  measurements at 35 mK – 1.1 K for (c)  $E_{IMP} = 80$  keV and  $T_{DA} = 700$  °C and (d)  $E_{IMP} = 45$  keV and  $T_{DA} = 400$  °C. For all the measurements, the magnetic field is applied perpendicular to the sample surface.

= 45 keV, scaling analysis yielded  $z\nu = 2.58 \pm 0.46$  at the  $T = 1.55$ – $1.95$  K range, followed by  $z\nu = 0.29 \pm 0.01$  at the  $T = 2.15$ – $2.55$  K range. Similar analysis on a sample with  $E_{IMP} = 25$  keV led to  $z\nu$  of  $0.65 \pm 0.04$  at the  $T = 1.55$ – $1.95$  K and  $0.4 \pm 0.01$  at the  $T = 2.15$ – $2.55$  K (Supplemental Fig. S13 [29]). While these values do not establish a trend toward divergent dynamical critical exponents, the general  $z\nu$  behavior warrants further investigation into their SMT at near-zero temperatures and higher magnetic fields.

Another signature of anomaly was observed in Ge:Ga samples when  $B_c$  temperature dependence was measured at mK temperatures (i.e., 35 mK–1.1 K). As shown in Figs. 7(c) and 7(d), both samples with  $E_{IMP} = 80$  keV and  $T_{DA} = 700$  °C (c) and  $E_{IMP} = 45$  keV and  $T_{DA} = 400$  °C (d) show anomalous rises in  $B_c$  as temperatures approach 0 K. To evaluate the  $B_c(T)$  behavior over a wider temperature range,  $B_c$  vs  $T/T_c$  curves from 35 mK to  $T_c$  for the two samples are provided in the Supplemental Material (see Supplemental Fig. S14 [29]). The anomaly persists regardless of the definition used for  $B_c$ , including for fields at critical sheet resistances of  $R_c = 0.1 R_n$ ,  $0.5 R_n$ , and  $0.9 R_n$ . The  $B_c$  vs  $T$  upturn is yet another evidence of disorder in these systems. The more interesting feature is the difference between the  $B_c$  upturn between the two samples, from positive curvature in Fig. 7(c) to linear in Fig. 7(d). The positive curvature of  $B_c(T)$  can be explained by a model of SC island weakly coupled via the Josephson effect, in which the value of the  $B_c$  is determined by an interplay between the proximity effect and quantum phase fluctuations [44]. In turn, the linear  $B_c(T)$  anomaly has been recently attributed to vortex glass ground states and their ther-

mal fluctuations confined in a disordered 2D geometry [45]. This picture is once again in agreement with the tunability of the global SC phase in Ge:Ga through the variation of  $E_{\text{IMP}}$ ; sensitivity to quantum fluctuations vs thermal fluctuations may be tailored by the extent of Ga atoms' spatial confinement.

#### IV. SUMMARY AND CONCLUSION

To summarize, we demonstrated a pathway to tune the superconductivity in Ge:Ga thin films using  $\text{Ga}^+$  implantation energy ( $E_{\text{IMP}}$ ) as the main parameter. By systematically monitoring the structural and magneto-transport characteristics of Ge:Ga samples over a wide  $E_{\text{IMP}}\text{-}T_{\text{DA}}$  phase space, we determined the conditions to tune the critical superconductivity parameters (i.e.,  $T_{\text{c}}$ ,  $B_{\text{c}}$ ) to record high values for Ge:Ga thin films. Those include  $T_{\text{c},50\%}$  of 4.1 K and parallel  $B_{\text{c}}$  of 7.95 T measured for the pseudo-2D Ge:Ga prepared at  $E_{\text{IMP}} = 25$  keV. At mK temperatures, anomalous upturns in  $B_{\text{c}}(T)$  were observed for the first time in Ge:Ga films. While the origins of the anomaly is yet to be determined, we showed that its temperature dependence can be tuned by

implantation energy. Further investigations for films with very shallow implantation depths may be necessary to determine the exact nature of this behavior at near-zero temperatures. Furthermore, our results warrant investigations into tunability of disorder in Ge:Ga thin-film systems as test-beds for QPT studies as well as platforms for SC circuits with high kinetic inductance.

#### Data Availability

The data that support the findings of this study are available within the paper and the Supplemental Material. Additional data are available from the corresponding author on request.

#### ACKNOWLEDGMENTS

The authors thank Emanuel Tutuc and Fatemeh Barati for fruitful discussions. The NYU team is supported by AFOSR Grant No. FA9550-16-1-0348 and ARO Grant No. W911NF1810115. K.S. thanks Davood Shahjerdi and Edoardo Cuniberto for their assistance with the Raman spectroscopy measurements. J.Y. acknowledges funding from the ARO/LPS QuaCGR fellowship reference W911NF1810067.

- 
- [1] Y.-P. Shim and C. Tahan, *Nat. Commun.* **5**, 4225 (2014).  
 [2] Y.-P. Shim and C. Tahan, *IEEE J. Sel. Top. Quant. Electron.* **21**, 1 (2015).  
 [3] G. Scappucci, C. Kloeffer, F. A. Zwanenburg, D. Loss, M. Myronov, J.-J. Zhang, S. De Franceschi, G. Katsaros, and M. Veldhorst, *Nat. Rev. Mater.* (2020).  
 [4] R. Skrotzki, J. Fiedler, T. Herrmannsdörfer, V. Heera, M. Voelskow, A. Mücklich, B. Schmidt, W. Skorupa, G. Gobsch, M. Helm *et al.*, *Appl. Phys. Lett.* **97**, 192505 (2010).  
 [5] B. Thorgrimsson, T. McJunkin, E. R. MacQuarrie, S. N. Coppersmith, and M. A. Eriksson, *J. Appl. Phys.* **127**, 215102 (2020).  
 [6] K. Sardashti, T. Nguyen, M. Hatefipour, W. L. Sarney, J. Yuan, W. Mayer, K. Kisslinger, and J. Shabani, *Appl. Phys. Lett.* **118**, 073102 (2021).  
 [7] J. Fiedler, V. Heera, R. Skrotzki, T. Herrmannsdörfer, M. Voelskow, A. Mücklich, S. Facsko, H. Reuther, M. Perego, K.-H. Heinig *et al.*, *Phys. Rev. B* **85**, 134530 (2012).  
 [8] T. Herrmannsdörfer, V. Heera, O. Ignatchik, M. Uhlarz, A. Mücklich, M. Posselt, H. Reuther, B. Schmidt, K.-H. Heinig, W. Skorupa *et al.*, *Phys. Rev. Lett.* **102**, 217003 (2009).  
 [9] R. Skrotzki, T. Herrmannsdörfer, V. Heera, J. Fiedler, A. Mücklich, M. Helm, and J. Wosnitza, *Low Temp. Phys.* **37**, 877 (2011).  
 [10] S. Prucnal, V. Heera, R. Hübner, M. Wang, G. P. Mazur, M. J. Grzybowski, X. Qin, Y. Yuan, M. Voelskow, W. Skorupa *et al.*, *Phys. Rev. Mater.* **3**, 054802 (2019).  
 [11] M. L. Cohen, *Phys. Rev.* **134**, A511 (1964).  
 [12] X. Blase, E. Bustarret, C. Chapelier, T. Klein, and C. Marcenat, *Nat. Mater.* **8**, 375 (2009).  
 [13] R. W. Olesinski and G. J. Abbaschian, *Bull. Alloy Phase Diagrams* **6**, 258 (1985).  
 [14] B. Spivak, P. Oreto, and S. A. Kivelson, *Phys. Rev. B* **77**, 214523 (2008).  
 [15] S. John and T. C. Lubensky, *Phys. Rev. B* **34**, 4815 (1986).  
 [16] T. Herrmannsdörfer, R. Skrotzki, V. Heera, O. Ignatchik, M. Uhlarz, A. Mücklich, M. Posselt, B. Schmidt, K.-H. Heinig, W. Skorupa *et al.*, *Supercond. Sci. Technol.* **23**, 034007 (2010).  
 [17] V. Heera, J. Fiedler, M. Naumann, R. Skrotzki, S. Kölling, L. Wilde, T. Herrmannsdörfer, W. Skorupa, J. Wosnitza, and M. Helm, *Supercond. Sci. Technol.* **27**, 055025 (2014).  
 [18] S. Eley, S. Gopalakrishnan, P. M. Goldbart, and N. Mason, *Nat. Phys.* **8**, 59 (2012).  
 [19] Y. Xing, H.-M. Zhang, H.-L. Fu, H. Liu, Y. Sun, J.-P. Peng, F. Wang, X. Lin, X.-C. Ma, Q.-K. Xue *et al.*, *Science* **350**, 542 (2015).  
 [20] Y. Saito, T. Nojima, and Y. Iwasa, *Nat. Commun.* **9**, 778 (2018).  
 [21] T. M. Hazard, A. Gyenis, A. Di Paolo, A. T. Asfaw, S. A. Lyon, A. Blais, and A. A. Houck, *Phys. Rev. Lett.* **122**, 010504 (2019).  
 [22] D. Niepce, J. Burnett, and J. Bylander, *Phys. Rev. Appl.* **11**, 044014 (2019).  
 [23] N. Samkharadze, A. Bruno, P. Scarlino, G. Zheng, D. P. DiVincenzo, L. DiCarlo, and L. M. K. Vandersypen, *Phys. Rev. Appl.* **5**, 044004 (2016).  
 [24] J. T. Peltonen, P. C. J. J. Coumou, Z. H. Peng, T. M. Klapwijk, J. S. Tsai, and O. V. Astafiev, *Sci. Rep.* **8**, 10033 (2018).  
 [25] O. V. Astafiev, L. B. Ioffe, S. Kafanov, Y. A. Pashkin, K. Y. Arutyunov, D. Shahar, O. Cohen, and J. S. Tsai, *Nature* **484**, 355 (2012).  
 [26] D. Campanini, Z. Diao, and A. Rydh, *Phys. Rev. B* **97**, 184517 (2018).  
 [27] J. F. Ziegler, *The Stopping and Ranges of Ions in Matter: Handbook of Stopping Cross-Sections for Energetic Ions in All Elements* (Elsevier, New York, 2013).  
 [28] J. Fiedler, V. Heera, R. Skrotzki, T. Herrmannsdörfer, M. Voelskow, A. Mücklich, S. Oswald, B. Schmidt, W. Skorupa, G. Gobsch *et al.*, *Phys. Rev. B* **83**, 214504 (2011).



- [29] See Supplemental Material at <http://link.aps.org/supplemental/10.1103/PhysRevMaterials.5.064802> for additional details on resistivity measurements, Hall measurements, structural characterization of the Ge:Ga films, temperature dependence of critical magnetic field in all superconducting Ge:Ga samples, as well as finite-size scaling analysis.
- [30] G. Deutscher, I. Grave, and S. Alexander, *Phys. Rev. Lett.* **48**, 1497 (1982).
- [31] C. J. Lobb, D. W. Abraham, and M. Tinkham, *Phys. Rev. B* **27**, 150 (1983).
- [32] S. Eley, S. Gopalakrishnan, P. M. Goldbart, and N. Mason, *J. Phys.: Condens. Matter* **25**, 445701 (2013).
- [33] D. W. Abraham, C. J. Lobb, M. Tinkham, and T. M. Klapwijk, *Phys. Rev. B* **26**, 5268 (1982).
- [34] W. C. Johnson, J. B. Parson, and M. C. Crew, *J. Phys. Chem.* **36**, 2651 (1932).
- [35] M. P. A. Fisher, *Phys. Rev. B* **36**, 1917 (1987).
- [36] A. M. Clogston, *Phys. Rev. Lett.* **9**, 266 (1962).
- [37] B. S. Chandrasekhar, *Appl. Phys. Lett.* **1**, 7 (1962).
- [38] H. Nam, H. Chen, T. Liu, J. Kim, C. Zhang, J. Yong, T. R. Lemberger, P. A. Kratz, J. R. Kirtley, K. Moler *et al.*, *Proc. Natl. Acad. Sci. USA* **113**, 10513 (2016).
- [39] A. W. Tsen, B. Hunt, Y. D. Kim, Z. J. Yuan, S. Jia, R. J. Cava, J. Hone, P. Kim, C. R. Dean, and A. N. Pasupathy, *Nat. Phys.* **12**, 208 (2016).
- [40] Y. Liu, Z. Wang, P. Shan, Y. Tang, C. Liu, C. Chen, Y. Xing, Q. Wang, H. Liu, X. Lin *et al.*, *Nat. Commun.* **10**, 3633 (2019).
- [41] C. Zhang, Y. Fan, Q. Chen, T. Wang, X. Liu, Q. Li, Y. Yin, and X. Li, *NPG Asia Mater.* **11**, 1 (2019).
- [42] N. Marković, C. Christiansen, and A. M. Goldman, *Phys. Rev. Lett.* **81**, 5217 (1998).
- [43] M. P. A. Fisher, P. B. Weichman, G. Grinstein, and D. S. Fisher, *Phys. Rev. B* **40**, 546 (1989).
- [44] V. M. Galitski and A. I. Larkin, *Phys. Rev. Lett.* **87**, 087001 (2001).
- [45] B. Sacépé, J. Seidemann, F. Gay, K. Davenport, A. Rogachev, M. Ovodnia, K. Michaeli, and M. V. Feigel'man, *Nat. Phys.* **15**, 48 (2019).